RPC Project Report

Monami Yoshioka, Winnie Liang, Arun Atwal

Summer 2023

Abstract

The ANUBIS (AN Underground Belayed In-Shaft) experiment in CERN foresees instrumenting the experimental cavern of the ATLAS experiment to search for long-lived particles using an array of resistive plate chambers (RPC). In this report we first use a scintillator setup with silicon photo-multipliers (SiPM) which are able to test the efficiency and performance of the scintillators and the RPC, by looking at the coincidences between the SiPMs within the same scintillator and between different scintillators and RPC. Furthermore, we test the performance of the RPC and the data-acquisition system (DAQ) through a series of tests involving the high-voltage system to test the leakage current of four different gases (argon, nitrogen, air and CO_2) as well as a mixture of argon and CO_2. We find the leakage current spikes around 1.4kV for argon, while nitrogen, air and CO_2 show a slower and exponential rise in current. When mixing the CO_2 with the argon we see that the CO_2 acts as a quenching gas for the argon, which is used as an ionising gas. Finally, the count rate of the RPC front-end boards (FEBs) was measured on the eta and phi sides of the RPC, as well as the combined count rate using the DAQ. We found that combining the eta and phi sides using a threshold voltage to only count events coming from both sides at the same time greatly reduced the effects of noise.

1 Introduction

1.1 ANUBIS project

The Standard Model of particle physics (SM) is an elegant theory that describes fundamental physics and has provided accurate predictions consistent with decades of experimental studies. However, there are still things that remain unanswered, and many SM extensions have been developed to address these problems. Some of these unsolved fundamental mysteries include the hierarchy problem, naturalness, dark matter, baryogenesis, and neutrino masses. They represent a possibility for physics beyond the standard model (BSM); Long-Lived Particles (LLPs) with macroscopic lifetimes emerge as natural predictions of these theories [1]. For example, a theory that naturally motivates LLPs is the supersymmetry theory (SUSY), which predicts a partner particle for each particle in the Standard Model with spin differing by 1/2, to help explain why particles have mass. Examples of several long-lived SUSY models are shown below.

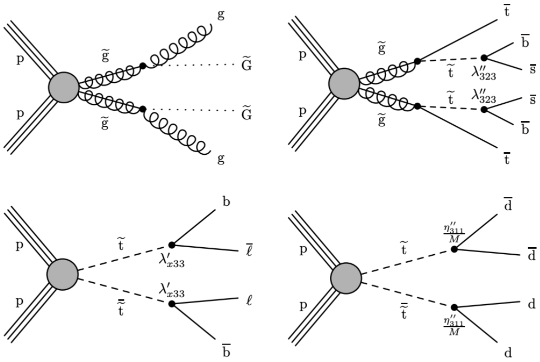

Figure 1: The Feynman diagrams for different long-lived SUSY models considered, including general gauge mediation with $\tilde{g} \to g\tilde{G}$ decay (upper left), RPV SUSY with $\tilde{g} \to tbs$ decay (upper right), RPV SUSY with $\tilde{t} \to$ bl decay (lower left), dynamical RPV SUSY with $\tilde{g} \to \overline{dd}$ decay (lower right) [2]

LLPs are particularly difficult to probe due to the limited sensitivity of LLPs of the main detectors at the Large Hadron Collider (LHC). AN Underground Belayed In-Shaft (ANUBIS) search experiment has recently been proposed [3] as a cost effective alternative to aid the LHC search for LLPs at CERN's ATLAS underground cavern. The main idea is to instrument the ceilings of the ATLAS cavern and the PX14 and PX16 service shafts, reducing civil engineering costs while providing LLP lifetime sensitivity to $0 < c\tau/m < 10^7$. Furthermore, it would allow the ANUBIS to trigger the readout of the ATLAS detector by fully integrating ANUBIS with ATLAS.

ANUBIS will use an indirect detection method to search for the LLPs, by detecting charged particles using the Resistive Plate Chamber (RPC) detector, and reconstructing the trajectories to go back to the vertex at the origin of these particles. Using the information collected by ATLAS, it can be determined if the particle at the origin of this vertex has been detected by ATLAS, and is therefore a known particle, or not, and is therefore possibly a new LLP particle.

In this report we use cosmic muons to perform various tests with one of the RPC singlets that will be used for the ANUBIS experiment. Section 2 will introduce all the detectors and technology that we use, in Section 3 we study the performance of the scintillators which are used to measure the efficiency of the RPC, and in Section 4 we will go in detail about the tests performed on the RPC.

2 Detectors and Experimental Setup

2.1 Silicon Photo-multipliers and Scintillators

A scintillator is a material that fluoresces when excited by ionising radiation. In this report we used EJ-200 scintillators of size 50cm x 50cm. EJ-200 combines the two important properties of long optical attenuation length and fast timing. Its photon emission spectrum is shown in Figure 2. The peak amplitude can be seen at a wavelength of 425nm.

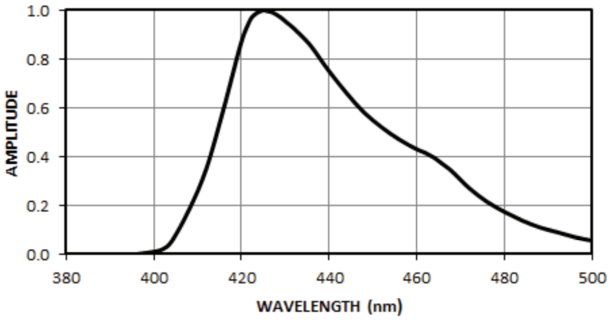

Figure 2: Photon emission spectrum for the EJ-200 scintillator [4].

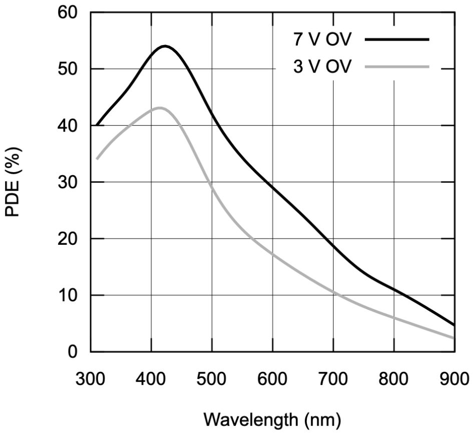

Figure 3: Spectral sensitivity of Broadcom AFBR-S4N33C013 SiPM [6].

When a charged particle (such as a cosmic muon) goes through the scintillator, photons are emitted. These photons are then intercepted by silicon photo-multipliers (SiPMs), which convert it into an output signal with a high gain. SiPMs are solid state single-photon-sensitive devices based on Single Photon Avalanche Diodes (SPAD). The photons emitted in the scintillators are absorbed by the silicon photodiodes in the SiPM, and create electron-hole pairs. By applying a bias voltage, a sufficiently high electric field is generated within the depletion region of the silicon, which accelerates a charge carrier so that it carries sufficient kinetic energy to create secondary charge pairs through impact ionization, and so on. Hence a single photon can trigger a ionisation cascade and create a measurable macroscopic current. The SiPM can detect multiple photons at a time by subdividing its area into multiple independent microcells. Hence the output is discretised into multiple photo-electron peaks as seen below.

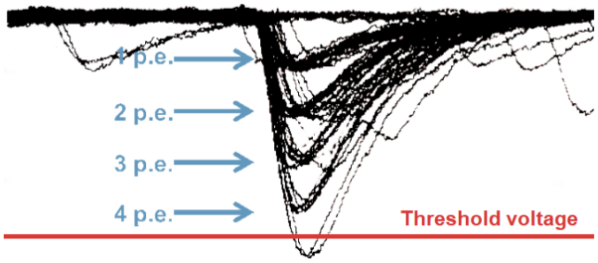

Figure 4: Oscilloscope shot (from [5]) showing the discrete nature of the SiPM output. A threshold voltage can be set to only accept peaks of certain amplitude.

An important thing to consider with SiPMs is the dark count rate (DCR), which is the main source of noise.

It is primarily due to thermal electrons generated in the active volume, as they can initiate an avalanche in the high field region. The signals produced by the electrons, whether they are photon-generated or thermally-generated, are identical. Therefore, thermally-generated electrons generate noise at the single photon level. To reduce the false triggers from the noise, a threshold can be set to only accept peaks below the threshold.

In this project we use Broadcom AFBR-S4N33C013 SiPMs, which have a spectral sensitivity as shown in Figure 3. The maximum PDE occurs at a wavelength of 420nm-425nm. This coincides with the photon emission spectrum for the EJ-200 scintillator, which means that the emitted wavelength matches with the wavelength at which the sensitivity of the SiPM is maximised.

The SiPM's dimensions are 3mm × 3mm, and are soldered onto a small PCB which contains an amplifying circuit. There are six wires in total soldered onto the PCB: VCC, AOUT, VBIAS and three GND wires. VCC is a $\sim$6.0V DC supply which powers the read-out electronics. AOUT is the output wire transmitting the SiPM signals to the coincidence board. VBIAS supplies the $\sim$32V bias voltage.

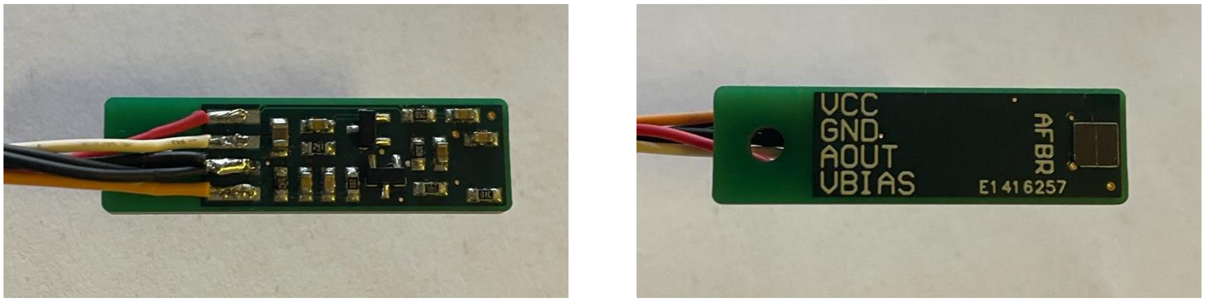

(a) Front of the PCB showing the amplifying circuit.

(b) Back of the PCB showing the 3mm x 3mm SiPM at the end of the board.

Figure 5: Photograph taken of the SiPM on the PCB, which amplifies the signal and sends it to the coincidence board.

2.2 Resistive Plate Chamber detectors

A Resistive Plate Chamber (RPC) is a particle detector widely used in high energy physics. They are used for detecting muons in most of modern experiments. It consists of two parallel electrode plates with high resistivity separated by a thin gas gap. A high potential difference is applied between the two plates. When a charged particle (such as a cosmic muon) goes through the gas gap of an RPC, it ionises the molecules and creates electron-ion pairs. The liberated electron may provoke further ionisation and a Townsend avalanche may develop. In Figure 6b, the mechanism behind the avalanche is shown: it is effectively a chain reaction with electrons. The electric field and the mean free path of the electron need to be such that it allows the free electrons to acquire certain energy that causes impact ionisation. If the electric field is too low, the electrons do not have enough energy to cause ionisation. If the mean free path is too small the electron loses its energy in a series of non-ionisation events, and if the mean free path is too large the electron reaches the resistive plates without interacting with any molecules. Hence the choice of gas used within the gas gap of the RPC is of great importance. In this project we use the RPC in avalanche mode, where the development of further electrons is suppressed by adding small amounts of quenching gases, which may absorb the electrons and limit the current.

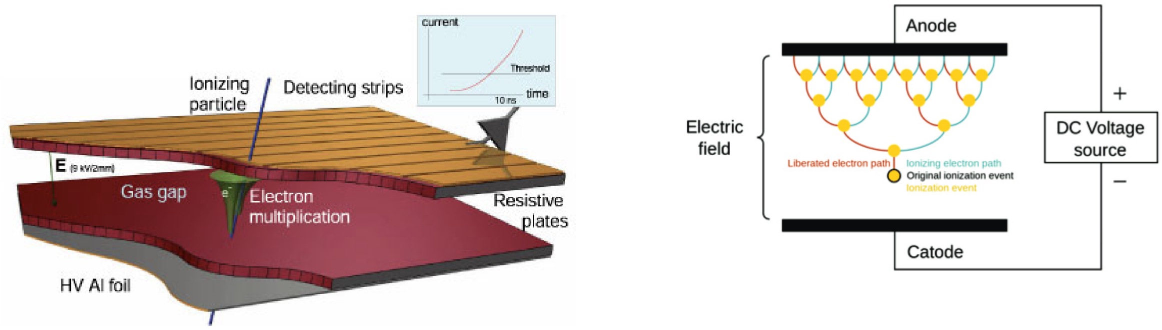

(a) Principle of operation of the RPC. [7]

(b) Townsend avalanche phenomenon. [8]

Figure 6: Diagrams showing the RPC and electron avalanche formation.

We have a BIS7S RPC board that has dimensions 100cm (eta) x 180cm (phi). The eta side has 4 front-end boards (FEB) with 8 channels each, giving a total of 32 channels on the eta side, and the phi side has 8 FEBs, giving a total of 64 channels on the phi side. Whenever there is a charged particle such as a muon going through the RPC, movement of the charges in the gas gap is detected by one of the 32 strips in the eta side and 64 strips in the phi side. As the electrodes are made of a resistive material, the drop in the electric field is contained locally in the position of ionisation and keeps the rest of the volume sensitive to the passage of other charged particles. The FEB processes the signal, which is then sent out via the channels. These channels are connected to a data acquisition system (DAQ), which is shown in Figure 7. A more in depth overview of the RPC and DAQ setup is covered in Section 4, 'Study of the RPC Detector'.

Figure 7: The data acquisition system containing all the boards. The silver strip connects to the FEBs on the RPC.

2.3 Overview of the experimental setup

Our task is to use a trigger setup to measure the performance parameters of the RPC. Two scintillators are used, one on top and one below the RPC, to determine the efficiency by looking at the coincidences of cosmic muon detection between them. First of all, however, we perform tests of the trigger setup using three scintillators, by determining the efficiency and performance of the third scintillator. The results are shown in Section 3, 'Study of Scintillators'. The results of the RPC tests are shown in Section 4, 'Study of the RPC Detector'.

The trigger setup is shown in Figure 8. It consists of two scintillators stacked on top of each other, held together by a metallic frame, and a third scintillator (or an RPC) in between. The scintillators are placed inside metallic trays secured to the frame, which have lids to isolate the scintillators from light. The separation and height of the metallic trays can be adjusted using screws attached to the side of the frame, and the electronics are placed at the bottom of the frame on top of a plastic tray to prevent short circuiting. Two SiPMs can be attached per scintillator, which have 45 degree cuttings in two of the corners. It was determined that this position gave the highest count rate [9]. Coincidence logic as shown in the Figure can then be applied to determine the efficiency of the object in the middle by seeing if a muon passing through the top and bottom plates also pass through the middle. The RPC-scintillator setup is very similar, but uses two scintillators with an RPC in the middle, which replaces the third scintillator. The signals from both the RPC and scintillators can be fed into the trigger boards in the DAQ for analysis and coincidence.

The electronics layout is shown in Figure 9. The SiPMs are soldered onto a PCB which amplifies the photo-electron and thermal-electron signals. Output signals of the SiPM PCB are sent to one of the four channels (A, B, C or D) that are found in the coincidence board, which are then connected to the computer via USB. The SiPMs require a 6.0V DC voltage supply, as well as the bias voltage. There are bias voltage generator boards which supply a fixed bias voltage of 32V, as well as adjustable bias voltage boards which lets you set the bias voltage by turning the potentiometer found on the board. The bias voltasge boards and the coincidence board need a ∼5.0V to power them.

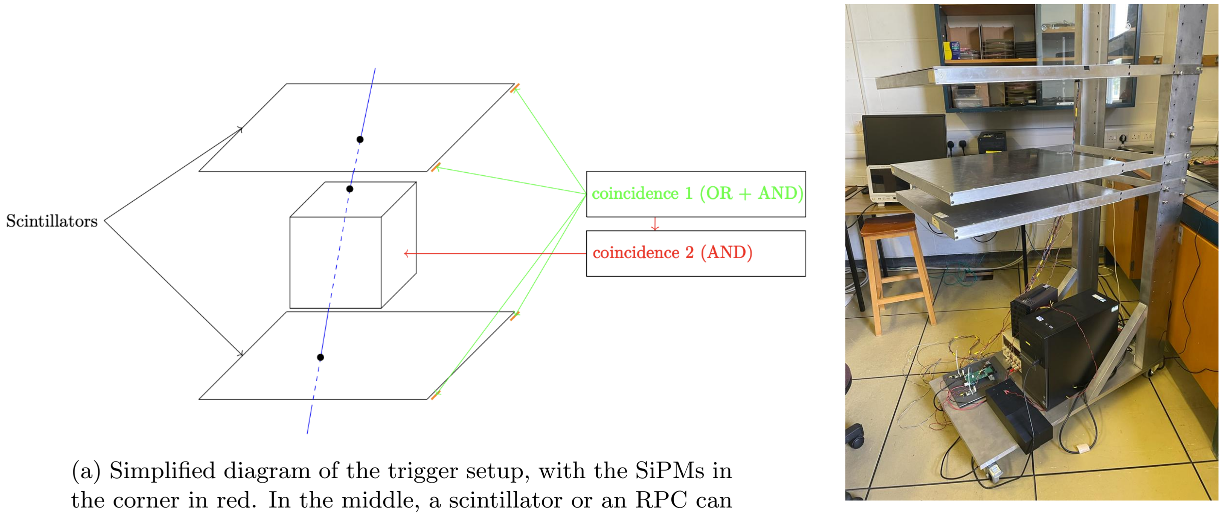

(a) Simplified diagram of the trigger setup, with the SiPMs in the corner in red. In the middle, a scintillator or an RPC can be placed. Diagram from [9]

(b) Scintillator trolley.

Figure 8: Scintillator setup

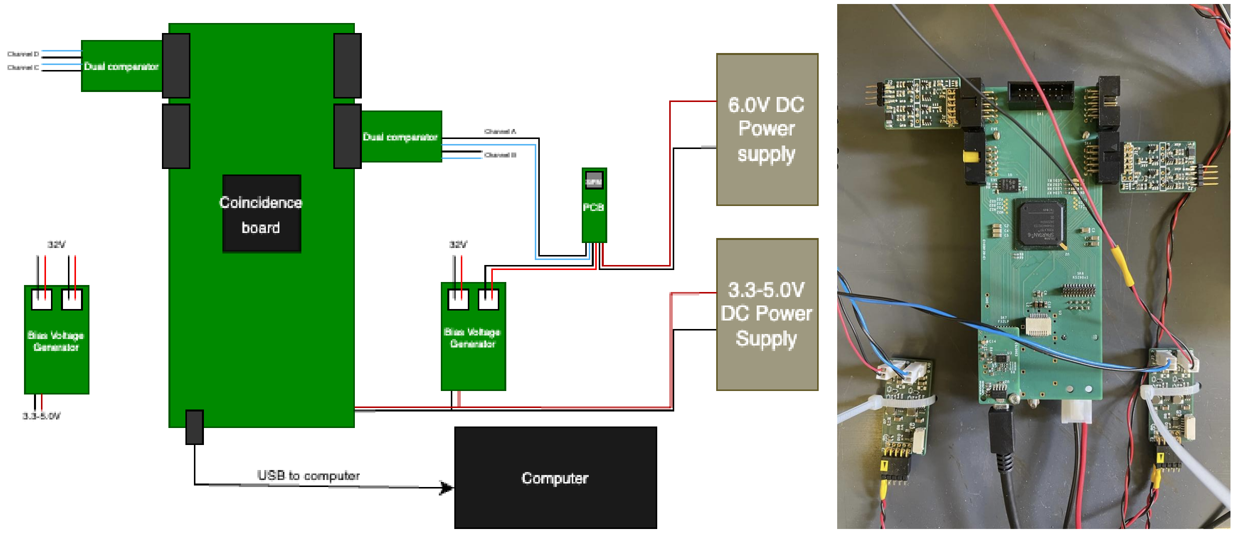

(a) Diagram of the electronics connections. (b) Photograph of the electronics.

Figure 9: Electronics setup

3 Study of the Scintillators

3.1 Checking the SiPM signals with the oscilloscope

First we made sure the SiPMs were working as expected by recording their DCR. We put each of the SiPMs inside a black bag to isolate them from light, and connected them to the oscilloscope. Most SiPMs showed multiple photon bands as expected. An example of a working SiPM is shown in Figure 10a, where you can clearly see the different bands corresponding to different number of electrons. The oscilloscope signal for SiPM 8 did not show the clear bands, and the noise was much higher, as seen in Figure 10b.

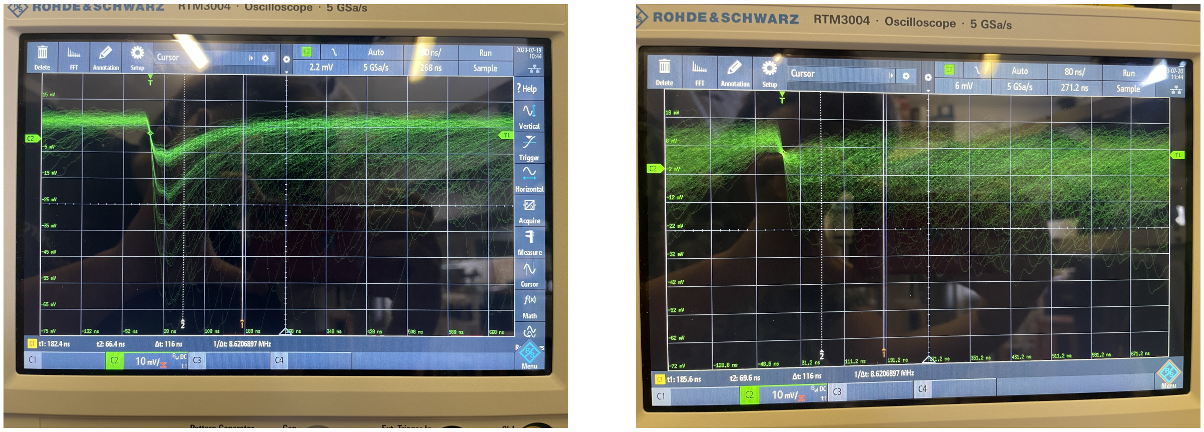

(a) SiPM 7. You can clearly see the bands corresponding to different number of photo-electrons.

(b) SiPM 8. The bands are not as clearly defined and noise is much higher.

Figure 10: Oscilloscope outputs for SiPMs 7 and 8 respectively.

We checked the SiPMs under the microscope to determine if there was any damage to the detector which might be causing this. We did not see any obvious damage so we kept using SiPM 8 in the following experiments, which might explain the low efficiencies and count rates that were seen in the next few sections that follow.

3.2 Threshold scan

Initially we performed a threshold voltage scan on SiPMs 6 and 9 from 600mV to 790mV in 10-20mV intervals. We measured the count rate of SiPM 6 and 9 individually as well as the coincidences of 6&&9. Both SiPMs were attached to Scintillator 3, with SiPM 9 connected to channel A and SiPM 6 connected to channel B. The results are shown in Figure 11.

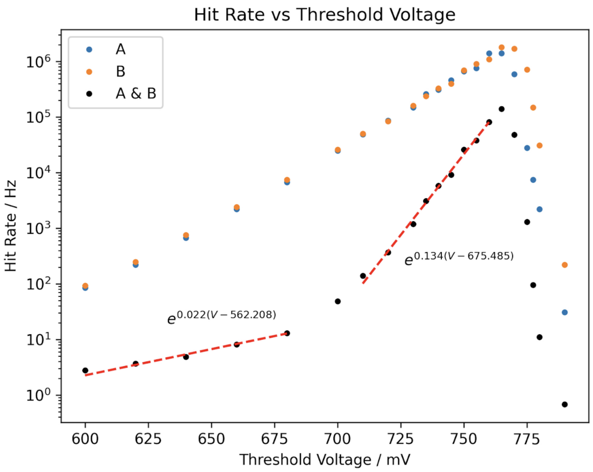

Figure 11: Variation of hit rate as threshold voltage scan is changed for SiPM 9 (channel A) and SiPM 6 (channel B) as well as coincidences of 6 and 9 combined.

As the threshold voltage is increased, we see that the count rate increases as we start to pick out more and more of the thermal noise. SiPMs 6 and 9 both exhibit very similar count rates, which is as expected as they are both connected to the same scintillator so there should not be huge variations. The plot for 6&&9 exhibits two coincidence regions. We can say that the coincidences below 690mV are mainly due to muons, while those higher would be from random coincidences due to the DCR. We made an exponential fit on the coincidence plot to to determine the ratio of random coincidences to muon coincidences. The exponential equations are shown on the figure. The ratios were found to be about 1:7.3 for 680mV and 1:6042 for 620mV.

We repeated the threshold scan with smaller steps of 2mV. This time we tested SiPMs 4, 7, 8 and 6, connected to channels A, B, C and D respectively. SiPMs 4 and 7 were attached to scintillator 1, SiPM 8 was attached to scintillator 2, and 6 was attached to scintillator 3.

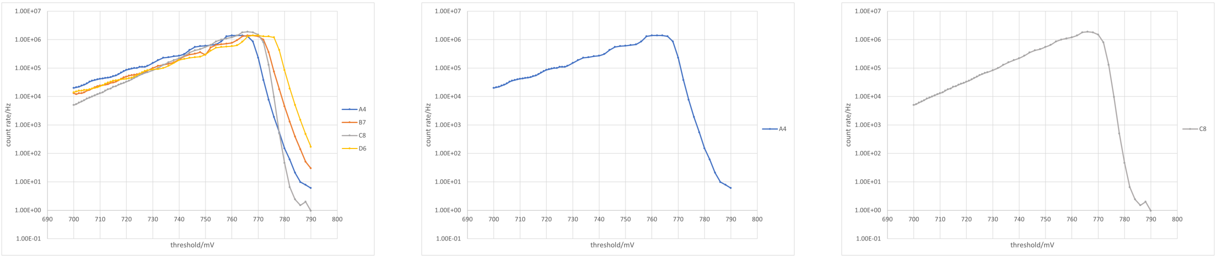

(a) SiPMs 4, 6, 7 and 8

(b) SiPM 4

(c) SiPM 8

Figure 12: Threshold scan for SiPMs 4, 6, 7 and 8

Figure 12a shows the results for all 4 SiPMs. Figure 12b shows the results for SiPM 4 alone, and Figure 12c shows the results for SiPM 8 to make it clearer to see. Error bars were added assuming Poisson noise.

As expected, we can observe steps in the count rate. These steps correspond to different numbers of photo-electrons being emitted, with one photo-electron at the peak, two photo-electrons on the next step, and so on with subsequent steps.

We find that SiPM 8's steps are hard to see. This might be caused by high amounts of electrical noise, which would smudge out the signal steps. This agrees with the oscilloscope readings from SiPM 8, which were very noisy electrically.

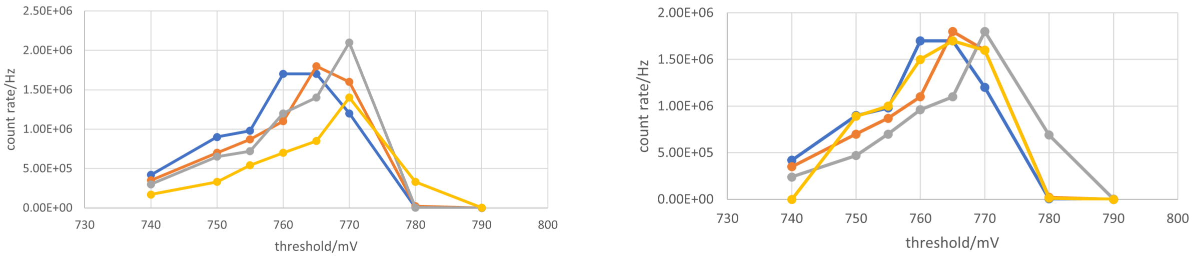

(a) Threshold scan of SiPM 6

(b) Threshold scan of SiPM 9

Figure 13: Effect of different channels on count rate

Furthermore, to see if the four channels behaved similarly, we did a threshold scan near the peak count rate (760mV) at the different channels. Using SiPMs 6 and 9 (both attached to scintillator 3), we measured the count rate while varying the threshold voltage for each of the 4 channels.

The results are shown in Figure 13. As expected, there is not much difference in the 4 channels, and all of the peaks lie between 760 and 770mV. The slight shift in the positions of the peak can be due to an offset in the electronics of each channel. Hence we can safely assume that the channel each SiPM is connected to has no significant effect on the output.

3.3 Efficiency of scintillator

We now move onto studying the efficiency of the scintillators. We placed scintillator 3 between 1 (top) and 2 (bottom). The SiPMs were connected as follows:

SiPM	Channel	Scintillator
9	A	3
6	B	3
8	C	2
4	D	1

The threshold voltage of scintillators 1 and 2 was fixed at 650mV, while we varied the threshold voltage of scintillator 3 from 590mV to 750mV. This allows us to find the efficiency of scintillator 3 by using scintillators 1 and 2 as triggers. We found the efficiency of scintillator 3 using Equation 1, where 6, 9, 4 and 8 correspond to the number of hits recorded by each of the 4 SiPMs as stated above.

$$\frac{(6\|9)\ \&\&4\&\&8}{4\&\&8} \tag{1}$$

The results are shown in Figure 14. The efficiency rises to peak of 70% at a threshold voltage of around 710mV. At lower voltages, the efficiency is low because it is harder for a photo-electron to be registered as a hit. At higher threshold voltages the efficiency also drops because the effect of dark count rate becomes more significant.

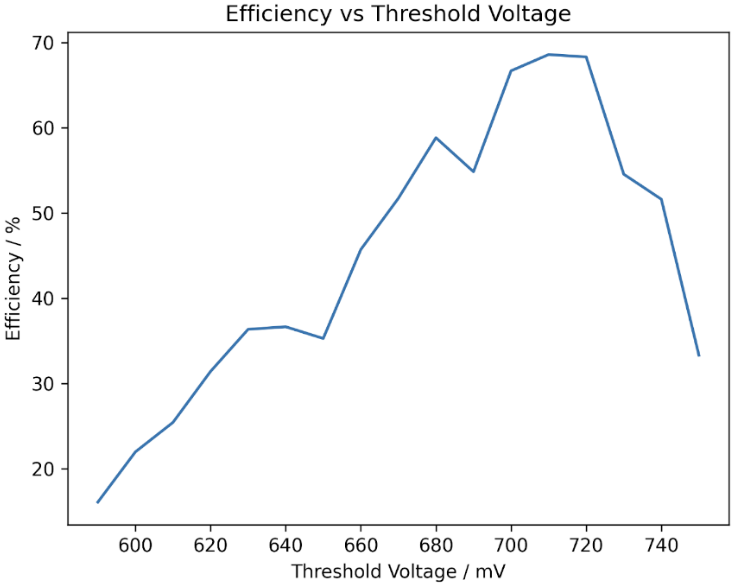

Figure 14: Variation of efficiency of scintillator 3 with threshold voltage

3.4 Effect of distance on the efficiency

Scintillator 3 was kept in place in the middle while the separation between scintillator 1 (top) and 2 (bottom) was changed from 20 cm to 100 cm. The SiPM connections are the same as the previous section. The efficiency of scintillator 3 was again found using Equation 1. We found the efficiency for a threshold voltage of 670mV, and then repeated the measurements for thresholds of 650mV (also within the muon dominant region but a lower count rate) and 690mV (starting to get into the region where dark count rate dominates).

Error bars were added, and error in each measured efficiency was calculated using the following:

$$\Delta\eta = \eta\sqrt{\left(\frac{\Delta\text{freq. of }(A\|B)\&\&C\&\&D)}{\text{freq. of }(A\|B)\&\&C\&\&D)}\right)^2 + \left(\frac{\Delta\text{freq. of }C\&\&D}{\text{freq. of }C\&\&D}\right)^2}$$

where η is the corresponding counts for each frequency and T is the data-logging time for each measurement, assuming $T = 0.5s$ and Poissonian noise, $\Delta\eta = \sqrt{\eta}$. The results are shown in Figure 15.

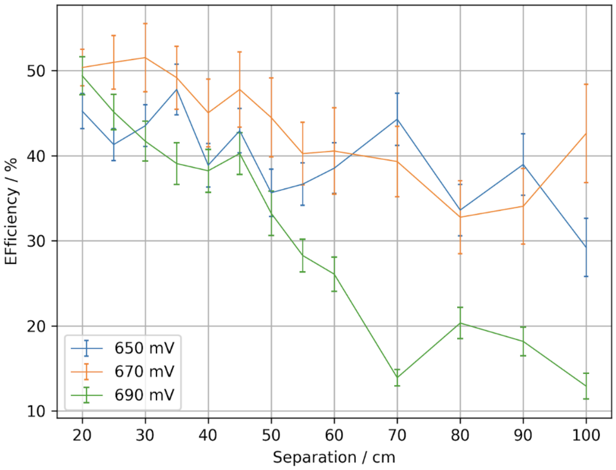

Figure 15: Efficiency of the trigger setup versus separation of the top and bottom scintillators for different threshold voltages

In general for all 3 voltages, efficiency dropped slightly with increasing separation. For 650mV and 670mV, the drop is less rapid. You would expect the efficiency to drop slightly as you increase the separation because the path length of the muon through the scintillator as well as the solid angle get shorter and smaller, and the fluctuation is mainly due to statistical variation. However, for 690mV, this rapid drop was not expected, since it is within the random count dominant region and the random counts are not expected to vary with separation. This behaviour seems to be repeatable, as performing the experiment again yielded the same results.

3.5 Effect of changing the bias voltage

A bias voltage scan was done for 3 different SiPMs on 3 different scintillators, in the voltage range around 26-37V. The SiPM connections are shown in the table below:

SiPM	Channel	Scintillator
8	A	2
9	B	3
7	C	1

In Figure 16a we compare the bias voltage scans of the three SiPMs. We observe a breakdown voltage of 31-32V (31.631V for SiPM 9 to be exact). This is much higher than the what was expected as seen in the Broadcom data sheet, which states a breakdown voltage of 26.9V. A graph showing the dark current as the bias voltage is varied was also provided, and is shown in Figure 16b.

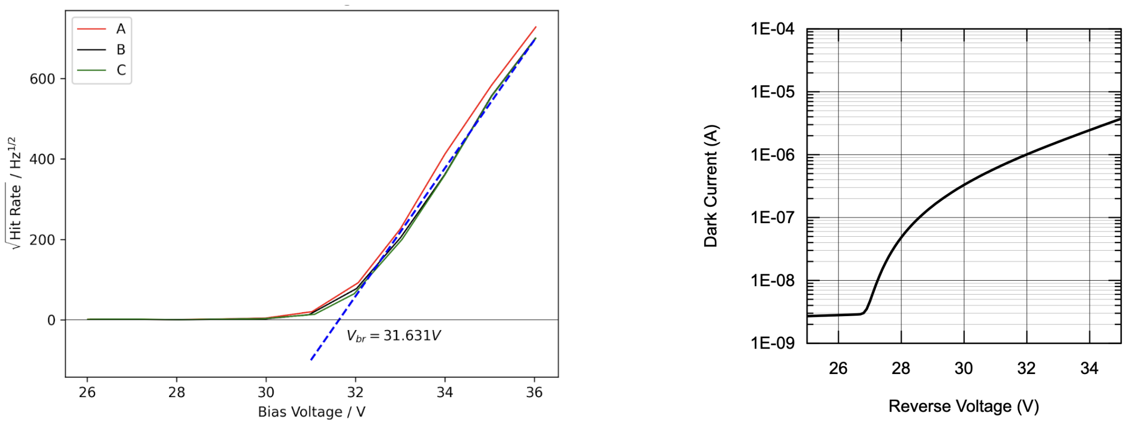

(a) Square root of the hit rate with respect to the bias voltage. We see a breakdown voltage of 31.631V.

(b) Dark current with respect to the bias (reverse) voltage. A lower breakdown voltage at 26.9V is shown.

Figure 16: Bias voltage comparisons between our data and the data found in the Broadcom SiPM datasheet.

4 Study of the RPC Detector

4.1 RPC and DAQ setup

There are tubes connecting from various gas canisters to the RPC which are used to select or mix different gases to flush through the RPC gas gap. Furthermore, the RPC has a high power voltage supply to set the voltage between the resistive plates, as well as a few low voltage supplies to power the FEBs and set discriminatory and threshold voltages. The FEBs on the RPC output data in the form of low voltage differential signals (LVDS) whenever there is a muon detected. These signals are sent to the trigger board found in the DAQ via flat cables, which are long strips of wires that carry 8 LVDS signal pairs each. There is one strip required per FEB, hence the eta side has up to 4 flat cables and the phi side has 8. The trigger board accepts 32 LVDS signal inputs, and contains a buffer that splits the incoming signal into two segments. The first segment is an exact copy of the signal which is outputted via a 32-channel connector for further use somewhere else in the DAQ. The second segment uses OR logic to convert the output to a TTL signal whenever there is a trigger in any one of the channels. The output if delivered through a LEMO connector. This TTL output can be then converted to an emitter-coupled logic (ECL) signal via the TTL-ECL converter board. The board uses the converted ECL signal and clock signal to generate an output signal that can be passed to the time to digital converter (TDC) via a flat cable. Finally, the CAEN TDCs use provide data for analysis by recording the time of particle interactions in the RPC detectors.

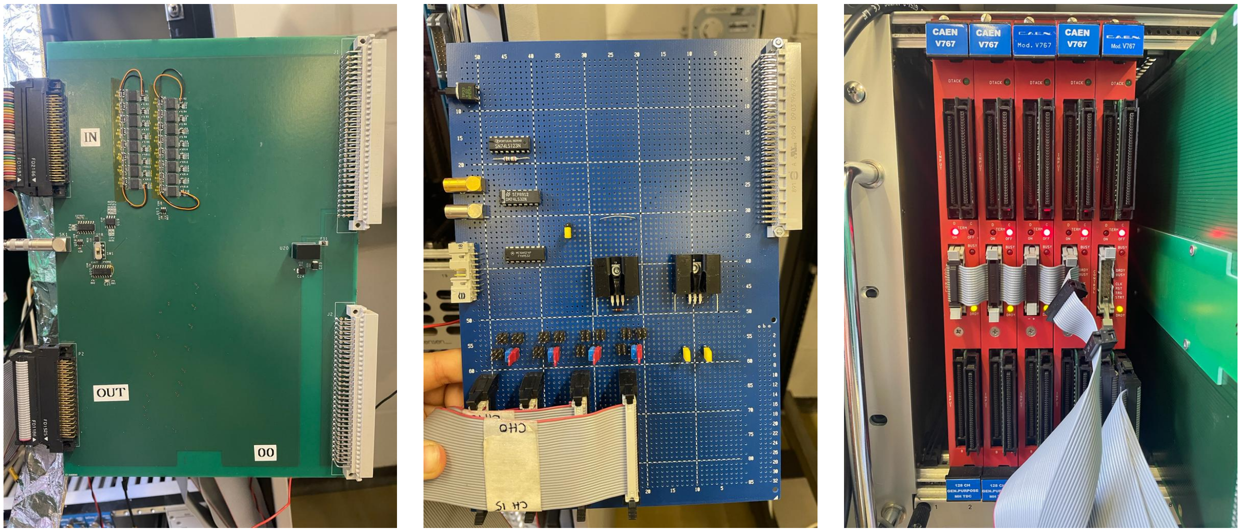

(a) Trigger board (b) TTL-ECL converter (c) CAEN modules

Figure 17: Boards used for the new experimental setup.

4.2 Effect of different gases on the leakage current

One of the most important aspects of an RPC is the choice of gaseous mixture. The choice of gas affects the amount of energy lost by a charged particle when it crosses the detector, as well the avalanche development and propagation. Usually a gas mixture in an RPC consists of three gases: an ionising gas which produces electrons ($\sim 95\%$), an UV quencher gas which prevents the development of secondary avalanches caused by a photon ($\sim 4\%$), and an electron quencher gas which is added to contain the avalanche and prevent it from spreading and developing too much ($\sim 1\%$) [7].

In the past, RPCs at CERN have used a Freon-based gas mixture containing $C_2H_2F_4$, SF_6 i-C_4H_{10}. $C_2H_2F_4$ and SF_6 are both greenhouse gases with a very high global warming potential (GWP), with GWP of 1430 and 29800 respectively [11]. However, F-Gases with a GWP of 150 or more will be limited or possibly even banned from 2025 onwards [12], as they are harmful to the environment. As a result, searching for alternative gases with lower GWP has become an important research field.

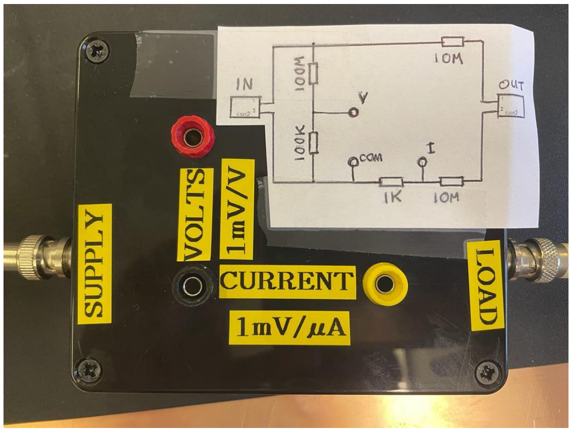

Figure 18: Box used to measure both current and voltage.

To start with, we performed IV (current-voltage) tests with four different gases: air, nitrogen, argon and CO_2. This was done to see the effect the different gases have on the leakage current while varying the voltage between the resistive plates, without connecting the low voltage supply or the DAQ. First, the gas would be flushed through the RPC for at least an hour to acclimatize, then the high voltage power supply was switched on and increased slowly from 0kV up to some high voltage up until we started hearing clicks from the RPC, which meant there were discharges occurring, or when we reached 4.0kV. A multimeter was used to measure both the voltage and the leakage current by plugging the probes into a box containing resistors, which is shown above. The results are seen in Figure 19. To compare the effect of the different gases further, the results have also been plotted in the same logarithmic graph in Figure 20.

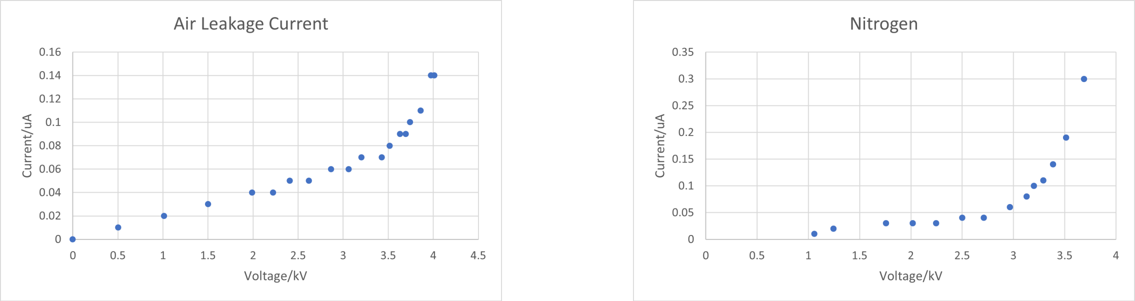

(a) RPC current-voltage characteristics for air (b) RPC current-voltage characteristics for nitrogen

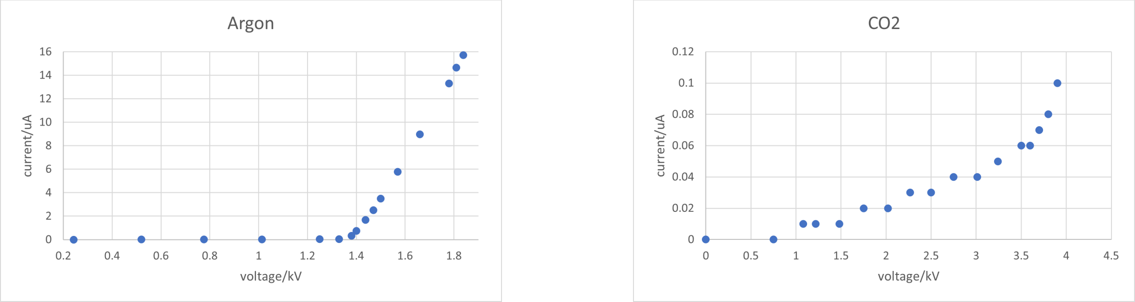

(c) RPC current-voltage characteristics for argon (d) RPC current-voltage characteristics for CO_2

Figure 19: Our measurements for the RPC current-voltage characteristics for different gases

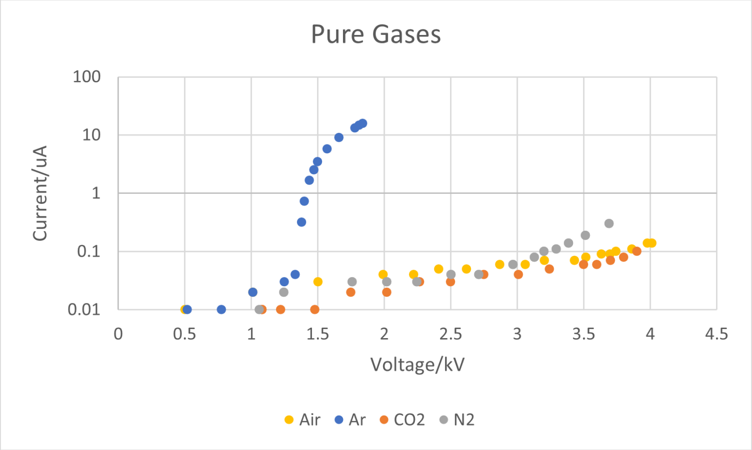

Figure 20: Leakage current of the four gases in the same logarithmic plot.

Air, nitrogen and CO_2 showcase similar relationships between current and voltage. Air and CO_2 especially show results that are very alike, which is interesting when considering the fact that air consists of 78.08% nitrogen; one would expect air and nitrogen to show the more similar behaviour. However, we can see that around 3.0kV, air and nitrogen plots begin to diverge. A theory we have come up with is that the nitrogen is a more ionizing gas, while CO_2 acts a quenching gas. Since air contains a mixture of nitrogen as well as oxygen (20.95%) and small traces of other gases (0.93% argon, 0.04% carbon dioxide) [13], the hypothesis is that the small traces of other gases mixed with the nitrogen act as quenchers and limit the electron avalanches from developing too much. It would be interesting to see the effect of mixing different proportions of nitrogen with CO_2.

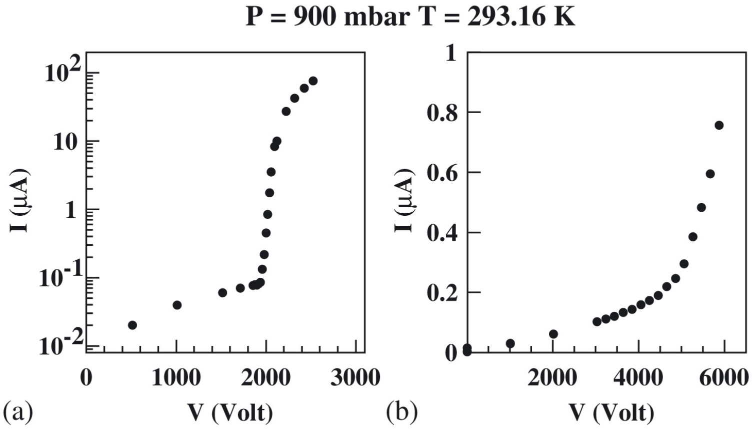

(a) (b)

Figure 21: RPC current-voltage characteristics in pure argon and in gas mixture Ar:i-C_4H_{10}:$C_2H_2F_4$:76:4:20 with additional 0.5% of SF_6

Looking at argon, we see a spike in leakage current at around 1.4kV. A report [14] was found which had done tests of the RPC with argon, shown in Figure 21a which confirms this observation. It can be seen that at low voltages, the dark current is linear with the voltage. Discharges begins in the gas when you increase the voltage further, and a spike in the current is observed at 2.0kV, due to the breakdown of the gas. The current is again linear with the voltage after this because the gas volume is practically short-circuited. The spike in current occurs at a higher voltage at 2.0kV compared with our spike which occurred at 1.4kV, due to the different RPC construction used. The general trend agrees with what we had seen in our IV test for Argon.

Furthermore, a leakage current test with a gas mixture (Ar:i-C_4H_{10}:$C_2H_2F_4$:76:4:20 with additional 0.5% of SF_6) was also performed in the same report. Figure 21b shows the IV characteristics for the gas mixture. This time, the gases added with the argon act as quenching gases, limiting the development of electron avalanches and hence a spike in the current is not seen. The trend in the graph is very similar to what is seen with nitrogen, air and CO_2.

We now delve into more detail to explain the different behaviours of the gases. First we consider the ionising potentials of the gases, which is the minimum energy required to remove the most loosely bound electron of an isolated gaseous atom. For an ionising gas used in an RPC, you would want a gas with low ionising potential to produce electrons. The ionising potentials are shown in the table below:

Nitrogen [15]	Argon [15]	CO_2 [16]
15.8eV	15.6eV	13.777eV

It is interesting that the ionising potential for CO_2 is the lowest, even though its leakage current is the lowest too. This suggests there is something else which helps determine the breakdown of gases, such as avalanche development and propagation. When an electron is freed by the passage of a muon, it drifts under the influence of the electric field and multiplies by interacting with gas molecules, leading to an electron avalanche that grows. For each electron, there is a possibility that it multiplies and creates adds more electrons to the avalanche, or it attaches to a gas molecule. Hence, assuming that the probability that an electron multiplies is independent of the previous position of multiplication, the avalanche can be characterised by a Townsend coefficient α and an attachment coefficient η. The probability that an electron multiplies is αdx the probability it attaches is ηdx for some small distance dx. If the avalanche contains n electrons at position x the probability that it contains $n+1$ electrons is at $x+dx$ is given by $n\alpha dx$. Following the same argument, the probability that for an avalanche of size n, one electron gets attached over distance dx is $n\eta dx$. Hence the change in the number of average electrons, $d\bar{n}$ and the change in the number of positive ions, $d\bar{p}$ is given by the following relationships:

$$d\bar{n} = (\alpha - \eta)\bar{n}dx, \quad d\bar{p} = \alpha\bar{n}$$

Note that the change in the number of electrons can be positive or negative depending on whether $\alpha < \eta$ or $\alpha > \eta$. In the case $\alpha = \eta$, the number of electrons is constant. Hence it is possible that $\alpha < \eta$ for CO_2, meaning more electrons attach to its molecules and do not continue multiplying to create avalanches. Below are two different graphs for CO_2 and a mixture of argon and O_2 showing the reduced effective ionisation coefficients $(\alpha - \eta/N)$ as a function of the reduced electric field strength. We observe that for CO_2 the effective ionization is less than zero until around 78Td, while pure argon's effective ionisation does not go under 0.

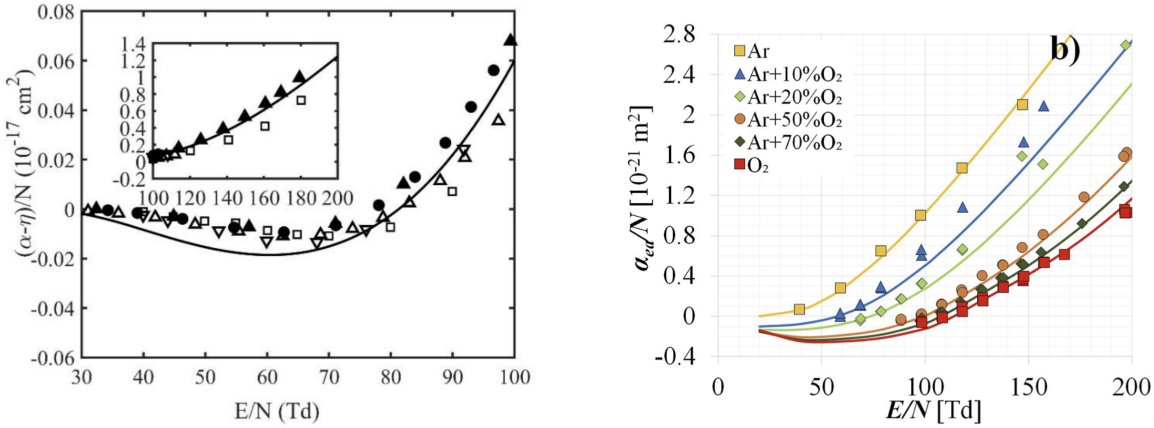

(a) The reduced effective ionisation coefficients in CO2 experimental (△, □), MAGBOLTZ (▽), BOLSIG+ (●), Boltzmann (▲) and present results (solid line).

(b) The apparent reduced effective ionization coefficient in mixtures with the composition varying from 100% Ar to 100% O_2, with solid lines calculates using BOLSIG+.

Figure 22: Reduced effective ionisation coefficients from two different sources, [17] (a) and [18] (b)

This leads us to tests performed by mixing various proportions of CO_2 and argon, to see whether CO_2 would act as a quenching gas and limit the leakage current when mixed with the argon. The test was performed by using flowmeters to set the flow rate of argon and CO_2 gas separately and then combining the flows together before feeding it in into the RPC. Note that the percentages stated are not accurate because the flowmeters were not calibrated for each gas (they were calibrated for air) and the resolution was low. However, the percentages still help to gain an approximate view of the performance of the argon-CO_2 mixture. We see again the spike in current for 100% argon at 1.4kV, and similar spikes emerging for ∼75% argon ∼25% CO_2 at 2.9kV. Once the argon content was low enough, the trend followed 100% CO_2. This suggests that the CO_2 is working well as a quencher. It would be beneficial to perform the test with more accurate measurements of the proportions of the gases: there is a big gap between the 100% argon and the mixtures, which could be due to the percentages being wrong meaning we did not test high ratios of argon to CO_2, or it could also imply that the quenching is effective even when adding very small amounts of CO_2.

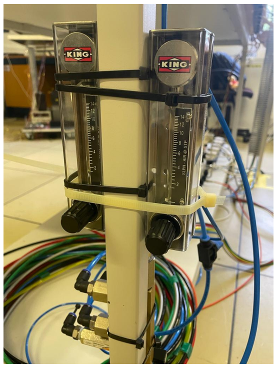

Figure 23: Flowmeters and valve setup which can be switched on and off to mix gases.

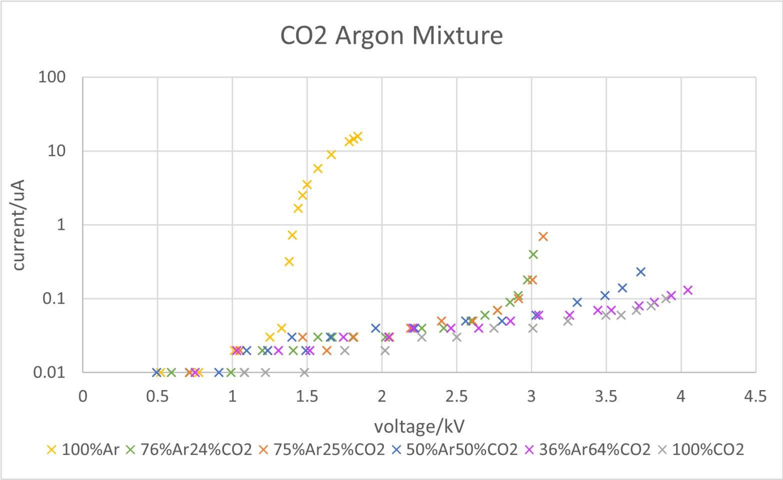

Figure 24: RPC current-voltage characteristics for a gas mixture of argon and CO_2 in different proportions.

4.3 Front-end board outputs

The FEBs have 6 coloured wires that are connected to the low voltage supply. The different wire's purposes and voltage levels are as follows:

Colour	Name	Voltage/V
Black	GND	-
Green	V_ LVDS	2.40
White	V_ Discriminator	2.50
Orange	V_ PullUp	0.35
Red	V_ Amplifier	1.30
Yellow	V_ Threshold	1.80

We turned on the low voltage supply to the front-end boards, and checked the signal output with the oscilloscope. When the high voltage is applied, you can see triggers corresponding to an event. The output is in the form of LVDS signal, hence we see that the voltages swap between differential pairs whenever a muon going through the RPC is detected, as seen in Figure 25a and 25b.

Once we have verified that the signals from the FEBs were as expected, we connected the output to the green board of the DAQ. The green board outputs a TTL trigger signal if any one of the channels detects a muon. Figure 25c shows the LVDS signal coming from the FEB in yellow and its corresponding trigger output shown in green.

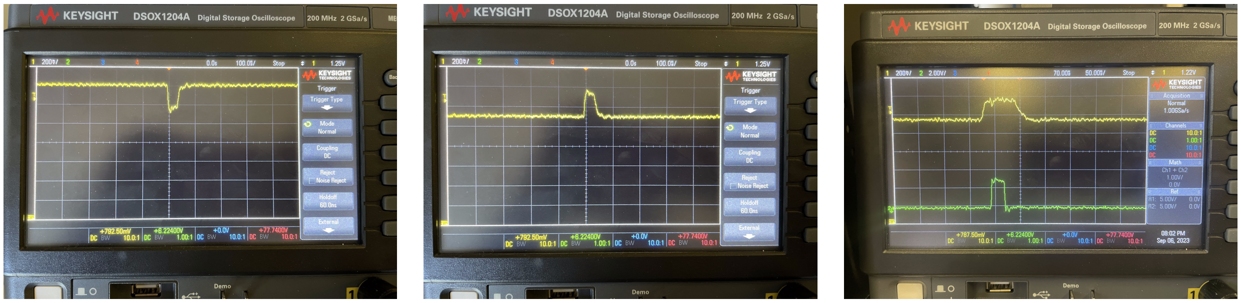

(a) Positive LVDS (b) Negative LVDS (c) LVDS and trigger output

Figure 25: Positive and negative LVDS signals from the FEB, and the LVDS signal (yellow) with its corresponding trigger output (green)

4.4 Measuring RPC count rates with CO2

It was found that the CAEN board in the DAQ which connects to the computer was not working, which meant we could not use the computer to directly analyse the data coming from the RPC. Two new boards were introduced: the Super OR (SOR) board and the TTL to NIM (Nuclear Instrumentation Mode) converter.

(a) Super OR board (b) TTL-NIM converter (c) Dual scaler

Figure 26: Boards used for the new experimental setup.

The SOR board accepts up to 6 input signals voltages in TTL format, and performs an analogue OR operation on the inputs. A threshold voltage can be set, which is used in the comparator unit on the board to only count a generated output if the analogue sum of the signals inputted is larger than the set threshold. To set the threshold, the board distributes 5V across the 6 inputs. For example, to combine the counts from the first two channels only, a threshold voltage of 0.83-1.67V would be set ($5 \div 6 \approx 0.83$, $0.83 \times 2 \approx 1.66$).

The TTL to NIM converter lets us convert the TTL signal coming from the trigger board or the SOR board into a NIM signal, which is then inputted into the dual scaler. This allows us to measure the count rates from the RPC. We can see in Figure 27 below a comparison between the LVDS, TTL and NIM signals. The updated experimental setup is shown in Figure 28.

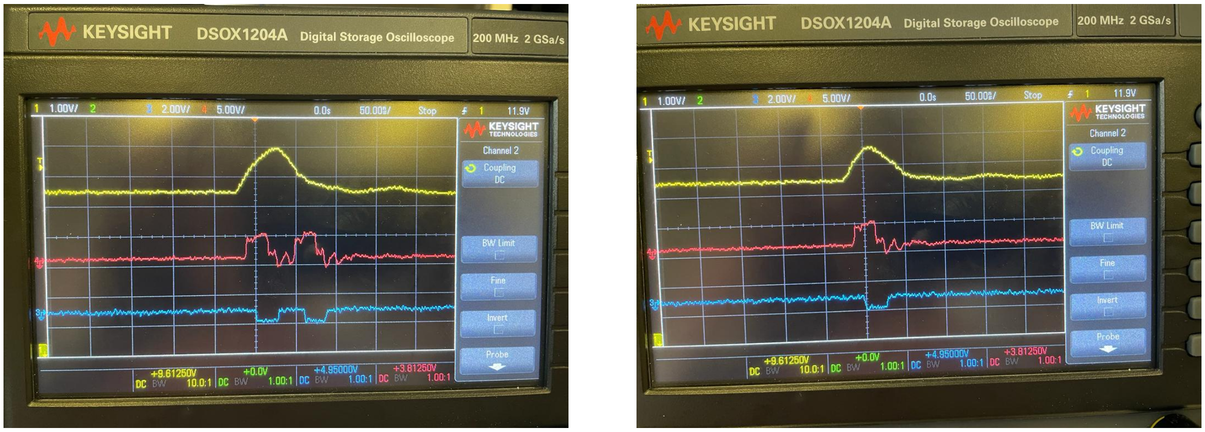

Figure 27: Two oscilloscope output examples of the LVDS signal (yellow), TTL signal (with no termination, red) and NIM signal (blue)

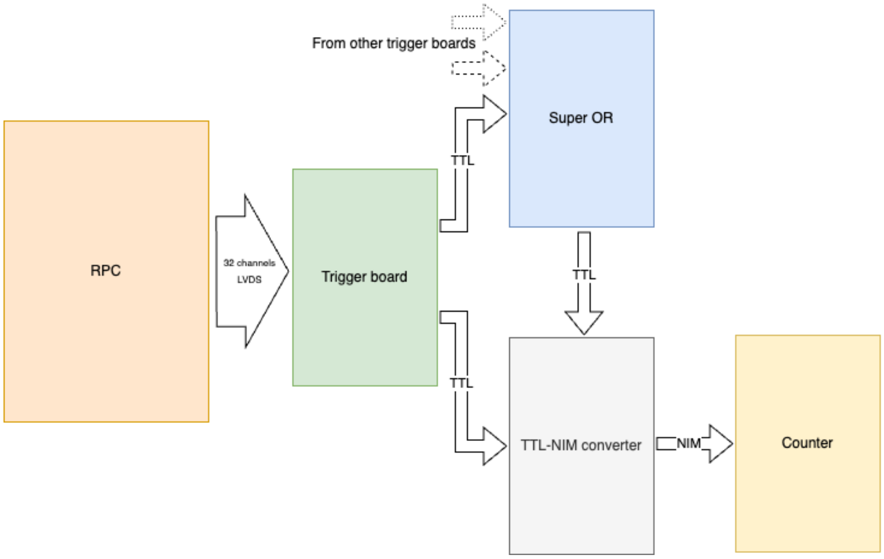

Figure 28: Flow chart of the new DAQ setup. The trigger signal can either go through the SOR board or straight to the TTL-NIM converter.

Using this setup, count rates from the eta side and phi sides were measured while varying the high voltage on two different dates, with CO_2 flushing in the RPC. This is shown in Figure 29a and b. Only 3 strips on the eta board were connected when the test was performed, as one of the channels was showing unusually high levels of noise. For the phi side, 4 out of the available 8 strips were connected for this test.

Errors where calculated assuming that the distribution of muon counts follows Poisson statistics, and that the error in measurement of time is dominated by human reaction time ($\Delta t \approx 0.3s$). The fractional error for a rate of count r is

$$(\frac{\Delta r}{r})^2 = (\frac{\sqrt{N}}{N})^2 + (\frac{\Delta t}{t})^2$$

where N is the number of muon counts within a period of time t, measured with a timer on the phone.

Run 1 and 2 were performed on the same day. In run 1, the TTL output from the trigger board of each side was directly passed through the TTL-NIM converter. In run 2, the trigger signal was first passed through the SOR board with a threshold of 0.6V, to see if the SOR board had any effect on the signal. From our results we can conclude that the SOR board has no effect on the signal when used as a 'pass-through' board.

We see almost no counts up until 2.5kV for both sides. After this, we see an increase in the count rate as the high voltage is increased, due to more of the disturbances of the gas ions being able to be detected when a muon passes through. Apart from the very low count rate seen on run 1 on the phi side (we realized a few days later that this was due to the connectors on the phi side being plugged in the wrong way around), the eta and phi count rates are similar to each other, with differences arising because there are less channels connected from the eta side but also the eta strips are longer than the phi strips. We noticed that the setup was very sensitive to noise, for example, from people moving around the RPC, stepping the ground and waving their hands over the FEBs. You can see this in the graphs from the multiple anomalous plots showing counts that are very high, which occurred whenever there was a sudden spike in the counts whenever we moved around too much or some other event contributed to the noise.

To explore this effect in more detail we performed the test again, this time by grounding ourselves using the grounding bracelets, and only having one person near the RPC to perform the counts. The new results are seen in run 3. We observe a much smoother rise in count rate with fewer anomalies, showing that grounding whenever possible is an important aspect in reducing the noise.

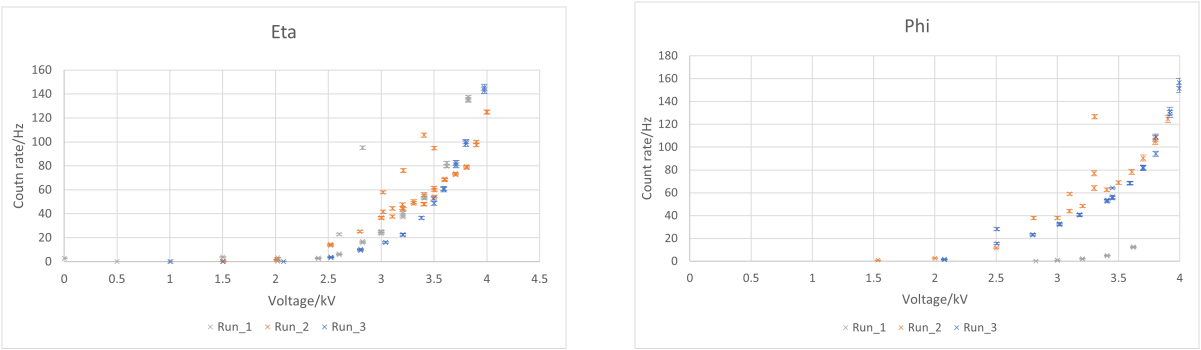

(a) Eta side.

(b) Phi side.

Figure 29: Muon count rates from single sides while varying high voltage. Grounding bracelets were used when doing the measurements in Run 3 only.

Moving on, the counts from the eta and phi sides were combined. The results are shown in Figure 30. The counts were combined by passing both the eta and phi trigger signals through the SOR board, and a threshold voltage was set between 0.83V and 1.67V to only perform a count if both eta and phi counts are observed. On the graph you can see 5 results taken on different days and with some slight variations in the setup between them.

For run 1 and run 2, thresholds of 1.001V and 1.313V were set respectively. We can see that the results are consistent with each other, showing that different threshold voltages have no effect if they are set between the intervals. We also noticed that the effect of noise was very much reduced due to the logic. However, the count rates were lower than we expected: taking into account that the muon flux rate is about 1 $\text{muon}\,\text{cm}^{-2}\,\text{min}^{-1}$ [19], we would expect on an RPC with area $180x100\text{cm}^2$ a muon count rate of around $18000/60 = 300$Hz. Run 1 and 2 showed over an order of magnitude smaller counts.

Again, we found that problem lay in the fact that the channel cables in the phi side were connected the wrong way around, which meant the signals were inverted so most of the trigger signals would not be converted to a TTL signal and hence not be included in the count. We ran the test again to confirm that the low count rate seen was due to the flipped channels; in run 3 we did not flip the cables and in run 4 we put them the wrong way around, as in run 1 and 2. The threshold set was 1.224V. We found that the count rate when the cables were connected the right way around (run 3) was much closer to the value we expected, although still slightly lower. We assume this is due to the multiple thresholding steps that the signal undergoes stopping some of the real muon signals from being included into the count, and furthermore not all of the muons would be able to ionise the gas molecules enough to create an electron avalanche. Run 4 shows the same behaviour as run 1 and 2, confirming that the direction the strips were connected was indeed affecting the count rate.

Furthermore, we reconnected the noisy 4th channel in the eta side and performed the same test again. This is seen in run 5. We expected to see a 33% increase in the count rate, as we are now considering coincidences between 4 strips instead of 3. We observe an increase of 60% $\sim$ 70% which is larger than expected, suggesting that noise still has an effect on the combined counts. However, this is probably due to the noisy channel: when connecting the noisy channel to the counter, the counter would instantly overflow and measure hundreds of thousands of counts in a second, which is clearly erroneous. The extremely high number of counts from the noisy channel most likely contributed to the combined count even though most of the counts were not real muon events.

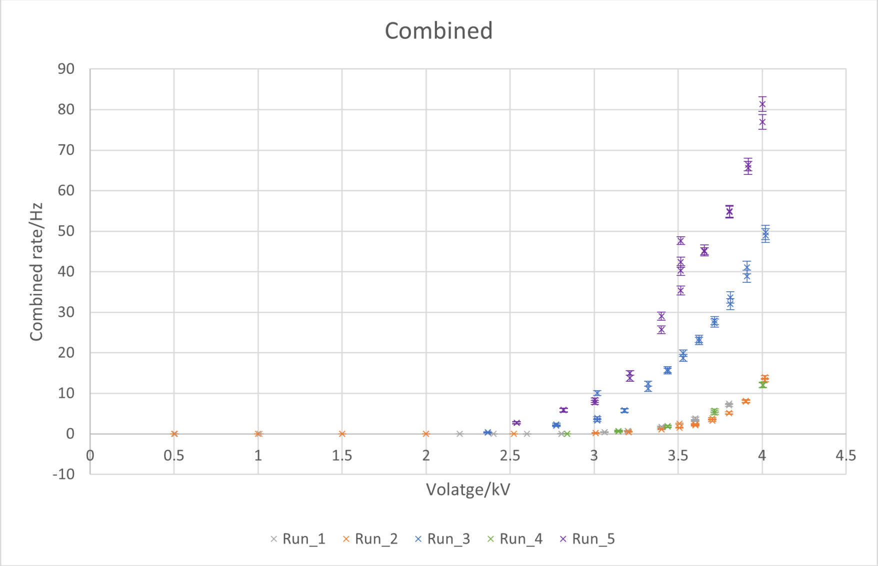

Figure 30: Combined count rates for phi and eta. In run 1, 2 and 4 the channel cables were flipped, in run 3 and 5 they were the right way around. The noisy 4th eta channel was only connected in Run 5.

After checking the connections, we found the problem with the noisy channel was that it was not grounded properly. We re-soldered the FEB ground connections and we found that the extreme amounts of noise had gone away, hence we performed the single counts test and the combined counts test again. This also helps to check that the results are reproducible. The results are shown below. We were pleased to see a smooth increase in the count rate as the high voltage is increases suggesting most of the noise had been removed, however we observe that the combined count rate had gone down to 80% of the value it was in on run 3, when we were expecting them to have the same count rates.

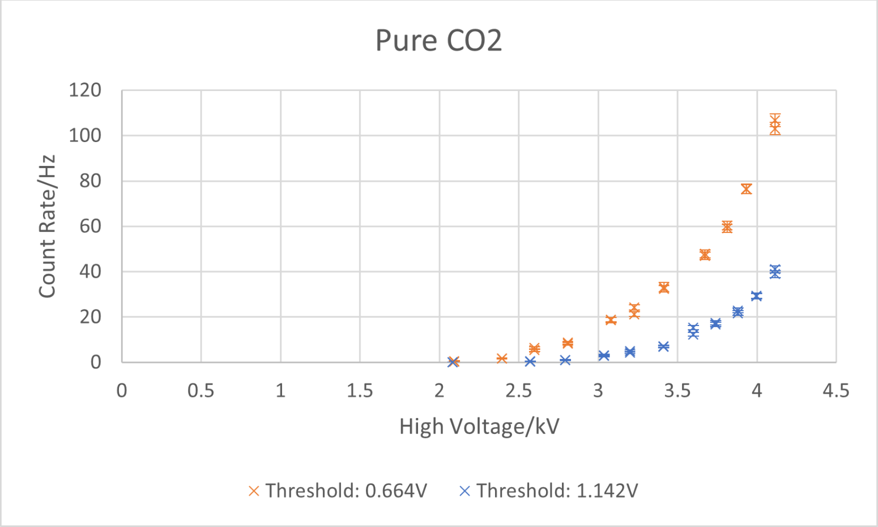

Figure 31: Combined count rate of eta and phi side through the SOR board.

4.5 Measuring RPC count rates with other gases

Finally, we performed the count rate test with nitrogen and with a mixture of argon and CO_2. When counting the eta and phi events for nitrogen, which is shown in Figure 32, we observe a higher count rate than with pure CO_2. This is not surprising considering that previously we have seen that nitrogen has a higher leakage current per given high voltage, as seen in Figure 20.

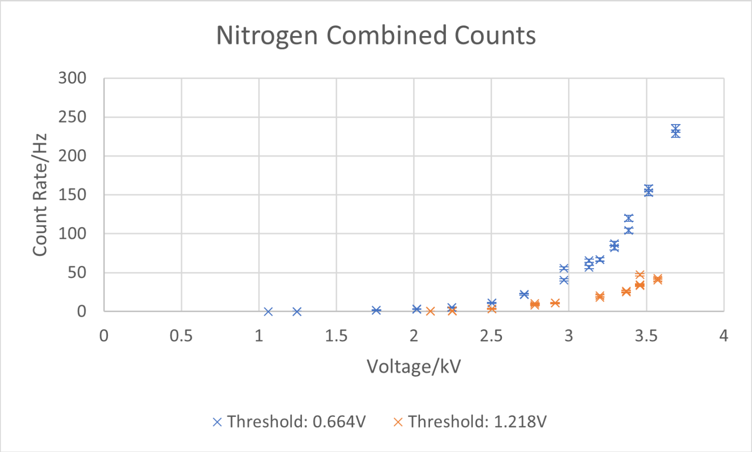

Figure 32: Combined count rates for phi and eta with pure nitrogen flushing in the RPC.

The leakage current for the mixture of argon and CO_2 was measured again, and at the same time the combined count rate was recorded by passing both eta and phi signals through the SOR board with a threshold of 1.2V. The results can be seen below. We see that around 2.7kV (for 80% argon- 20% CO_2) and 3.2kV (the rest of the mixtures) the leakage current starts spiking up, while the relationship between voltage and count rate becomes linear in the logarithmic graph (hence showing an exponential relationship). This suggests that although the leakage current explodes due to single events, the combined counts are all due to real muon events.

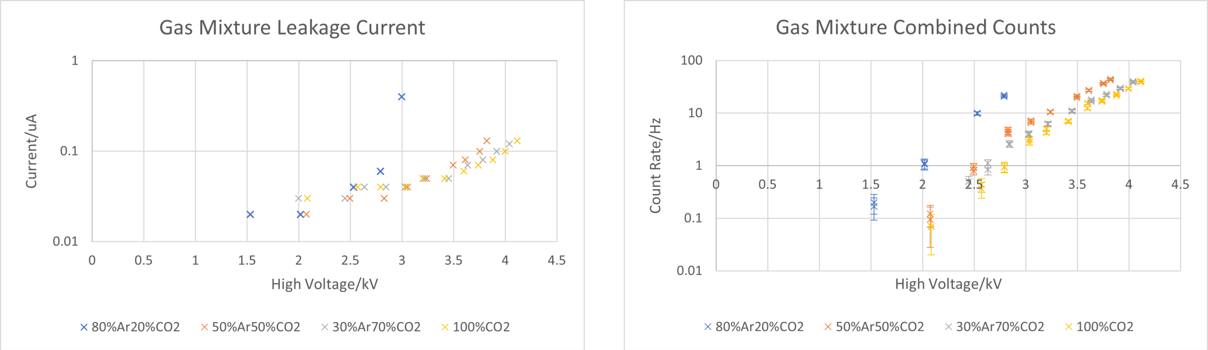

(a) Logarithmic graph of leakage current.

(b) Logarithmic graph of the combined count rate.

Figure 33: Tests performed with a mixture of argon and CO_2 in different proportions.

5 Conclusion

The ANUBIS project shows great potential in detecting new physics such as long-lived particles, and the RPC detector has been shown to be a crucial component in it. Throughout this project, we have taken steps to further understand the RPC with the goal of determining the efficiency using the scintillator trigger setup and eventually use an array of RPC detectors to trace back the trajectories of particles in the ceiling of ATLAS' experimental cavern.

We first tested the SiPMs and the scintillator setup by themselves. The oscilloscope outputs showed clear photo-electron bands for most of the SiPMs, although some seemed to be damaged as they showed large amounts of electrical noise. This encouraged a new design for the mounting and PCB, which is explored further in a separate report written for the new setup which was worked on by us in the same summer as this project. When performing a threshold voltage scan of the SiPMs attached to the three scintillators, we observe two regions when measuring the count rate: one region dominated by real muon counts and one region dominated by the dark count rate generated by noise from the thermal-electrons. Up until 680-690mV, the count rate was mostly dominated by muons, hence we chose a threshold voltage of 670mV for the experiments that followed to stay within the muon count region but also have a high enough count rate.

The efficiency of the third scintillator was also measured, which rose to a peak of 70% around a threshold voltage of 710mV. Furthermore, the distance between the scintillators was changed to determine the effect of distance on efficiency, where the distance seemed to affect the efficiency the most in the thermal-noise dominated regions.

Moving onto the study of the RPC, we tested the RPC leakage current by varying the voltage between the resistive plates with four different gases: air, nitrogen, argon and CO_2. It was found that while air, nitrogen and CO_2 showed slow exponential rise in the leakage current, argon's current spiked at 1.4kV. Research was done to conclude that the argon is used as an ionising gas, while small traces of other gases such as CO_2, which act as a quencher, limits the electron avalanche formation. When mixing argon and CO_2, we find that the leakage current does indeed fall as the proportion of CO_2 increases.

Finally the DAQ was integrated with the RPC to measure the muon count rate from the RPC, using CO_2, pure nitrogen and a mixture of argon and CO_2. First, the eta and phi sides were tested separately, and we found the effect of noise being reduced when grounding ourselves while taking the measurements. Furthermore, noise was greatly removed when combining the eta and phi counts together using the super-OR board to set a threshold voltage. We see a linear relationship in the logarithmic graph of the count rate and the voltage applied, which suggests that all of the counts are due to real muon events. Improvements of the setup have been suggested to use gas mixers to more accurately control the proportions and flow rates of the gas to be able to determine the effect of the different gases in more depth. These findings hopefully help provide some steps to help with determining the performance of the RPCs to be used in the ANUBIS experiment.

References

[1] David Curtin et al. (Mar 2019). *Long-Lived Particles at the Energy Frontier: The MATHUSLA Physics Case*. arXiv:1806.07396v2

[2] Jingyu Luo. (Sep 2019). *Search for Long-lived Particles Decaying into Displaced Jets with the CMS Detector at the Large Hadron Collider*. `http://arks.princeton.edu/ark:/88435/dsp013484zk83n`

[3] Martin Bauer et al. (Oct 2019) *ANUBIS: Proposal to search for long-lived neutral particles in CERN service shafts*. arXiv:1909.13022v2

[4] Eljen Technology (2021). *GENERAL PURPOSE PLASTIC SCINTILLATOR EJ-200, EJ-204, EJ-208, EJ-212* datasheet. `https://cernbox.cern.ch/index.php/s/YdLHKoHi8vlsynA`

[5] SensL, (2011). *An Introduction to the Silicon Photomultiplier*. `https://cernbox.cern.ch/index.php/s/1NSCluoAatGCMZu`

[6] Broadcom, (2022). *AFBR-S4N33C013 NUV-HD*. Single Silicon Photo Multiplier datasheet. `https://docs.broadcom.com/doc/AFBR-S4N33C013-DS`

[7] Français V. (2018) *Description and simulation of the physics of Resistive Plate Chambers*. `https://cernbox.cern.ch/index.php/s/rfmzIfEwTmpWYId`

[8] Psarra A. (2027) *Cosmic bitcasting/* `https://www.researchgate.net/figure/Townsend-avalanche-phenomenon_fig3_319589097`

[9] Reymermier, T. (2022). *Timing coincidence trigger setup*. Cavendish Laboratory, University of Cambridge

[10] European Comission (2023). *EU legislation to control F-gases*. `https://climate.ec.europa.eu/eu-action/fluorinated-greenhouse-gases/eu-legislation-control-f-gases_en`

[11] United Nations (). *Global Warming Potentials (IPCC Second Assessment Report)* `https://unfccc.int/process/transparency-and-reporting/greenhouse-gas-data/greenhouse-gas-data-unfccc/global-warming-potentials`

[12] R. Guilda et al. (April 2020) *Performance studies of RPC detectors with new environmentally friendly gas mixtures in presence of LHC-like radiation background*. `https://doi.org/10.1016/j.nima.2019.04.027`

[13] Haynes, H. M., ed. (2016–2017), CRC Handbook of Chemistry and Physics (97th ed.), CRC Press, p. 14-3, ISBN 978-1-4987-5428-6

[14] A. Bergnoli et al. (2004). *The quality control tests for the RPCs of the OPERA experiment*. `https://doi.org/10.1016/j.nima.2004.07.028`

[15] Clifton G. Found. *Ionization potentials of argon, nitrogen, carbon monoxide, helium, hydrogen, mercury and iodine vapors*. `https://journals.aps.org/pr/pdf/10.1103/PhysRev.16.41`

[16] NIST Chemistry WebBook (2023). *NIST Chemistry WebBook, SRD 69.*

`https://webbook.nist.gov/cgi/cbook.cgi?ID=C124389&Mask=20`

[17] Dincer et al. (2020). *Determination of Electron Swarm Parameters and Limiting Electrical Field during Martian Dust Storm Season Using Boltzmann Analysis*. Acta Physica Polonica A. 138. 368-376. 10.12693/APhysPolA.138.368.

[18] Talviste R. (2022). *Effective ionization coefficient in mixtures of Ar and O2 determined using the Townsend discharge*.

[19] J.L. Autran et al. (2018). *Characterization of atmospheric muons at sea level using a cosmic ray telescope*. `https://doi.org/10.1016/j.nima.2018.06.038`